

# CONTENTS

---

|        |                                     |    |
|--------|-------------------------------------|----|
| 1      | SED PROPERTIES                      | 1  |
| 1.1    | Introduction                        | 1  |
| 1.2    | Data                                | 2  |
| 1.2.1  | SDSS DR7                            | 2  |
| 1.2.2  | UKIDSS Large Area Survey            | 2  |
| 1.2.3  | WISE All-WISE Survey                | 3  |
| 1.2.4  | Quasar sample                       | 3  |
| 1.3    | Quasar SED                          | 4  |
| 1.4    | SED Model                           | 6  |
| 1.4.1  | Accretion Disc                      | 6  |
| 1.4.2  | Balmer Continuum                    | 6  |
| 1.4.3  | Hot Dust                            | 6  |
| 1.4.4  | Emission Lines                      | 6  |
| 1.4.5  | Host Galaxy                         | 7  |
| 1.4.6  | Dust Extinction                     | 8  |
| 1.5    | The ‘Standard’ SED Model            | 8  |
| 1.6    | Results                             | 10 |
| 1.7    | Discussion of Fit                   | 10 |
| 1.7.1  | Flux Correction                     | 14 |
| 1.8    | Hot Dust                            | 14 |
| 1.8.1  | Parametrising the hot dust emission | 14 |
| 1.8.2  | Sample                              | 16 |
| 1.8.3  | Diversity in hot dust properties    | 17 |
| 1.9    | Fitting procedure                   | 18 |
| 1.10   | Results                             | 19 |
| 1.10.1 | Correlations with quasar properties | 21 |
| 1.10.2 | Spectral properties                 | 21 |
| 1.11   | Discussion                          | 22 |
| 1.11.1 | Eddington ratio                     | 26 |
| 1.12   | Further work                        | 27 |

## LIST OF FIGURES

---

|            |   |
|------------|---|
| Figure 1.1 | Median radio-loud SED from Shang et al., (2011). 2  |
| Figure 1.2 | Distribution of our sample in the redshift-luminosity plane. 4  |
| Figure 1.3 | Model spectrum at $z = 1$ , showing the contributions to the total flux from the blue power-law slope, red power-law slope, Balmer continuum, blackbody, emission line spectrum and host galaxy 5   |
| Figure 1.4 | Model spectrum at three different redshifts (each arbitrarily scaled), and throughput functions for SDSS, UKIDSS and WISE band-passes. 9  |
| Figure 1.5 | Colours of median SED and best-fitting model, with and without correction. <b>Corrected is in orange, uncorrected in green. Check with Paul. Correction often makes colours a lot worse. Once got to the bottom of this just show with correction.</b> 11 |
| Figure 1.6 | Colours of median SED ( <i>black circles</i> ), individual objects ( <i>grey points</i> ), best-fitting model ( <i>black line</i> ) as a function of redshift. 12   |
| Figure 1.7 | Residuals from fit as a function of rest-frame wavelength. <b>Show before and after correction.</b> 13  |
| Figure 1.8 | Ratio of NIR to UV luminosity ( $R_{\text{NIR/UV}}$ ) against temperature ( $T_{\text{BB}}$ ) for low- $z$ sample. The density of points is shown in more dense regions of the space, and individual objects in less dense regions. 15                    |
| Figure 1.9 | $i - K$ colours of non-BALQSO DR7Q quasars with $i > 19.1$ as a function of redshift. The lines show the colours of our model with varying amounts of dust extinction. Quasars with extinction $ E(B - V)  > 0.075$ are excluded. 17                      |

- Figure 1.10 W1 – W2 colours of sample as a function of redshift. Above a certain density threshold points are represented by a density plot. On top we plot the colours of our standard SED model, with a fixed temperature and a varying NIR (1 - 3  $\mu\text{m}$ ) to UV ratio. 18
- Figure 1.11 Ratio of NIR to UV luminosity ( $R_{\text{NIR/UV}}$ ) against temperature ( $T_{\text{BB}}$ ). The grey contours show equally-spaced lines of constant probability density generated using a Gaussian kernel-density estimator on our data sample. The black points are for our mock data. 19
- Figure 1.12 Best-fit black-body temperature against UV luminosity (left), black-hole mass (centre) and Eddington ratio (right) for  $1 < z < 1.5$  sample (black) and  $2 < z < 2.7$  sample (black). In region of high-density we represent the density with contours generated using a Gaussian kernel density estimation. Needs re-making with new BH masses. 20
- Figure 1.13 Composite SDSS spectra for objects at  $z \sim 0.7$ . We have divided sample into objects with objects best-fit by small (red line) and large (red line) values of  $\beta$ . Remake if possible. 22
- Figure 1.14 Rest-frame equivalent width and blueshift of the C IV line for 7,115 SDSS DR7 quasars. The colours of the hexagons denote the median hot dust ( $T \simeq 1200 \text{ K}$ ) abundance for all quasars at a given equivalent width and blueshift. Quasars with the most extreme outflow signatures are predominantly hot-dust rich. Only bins containing a minimum of two objects are plotted. 23
- Figure 1.15 Rest-frame equivalent width and blueshift of the C IV line for 7,115 SDSS DR7 quasars. The colours of the hexagons denote the median hot dust ( $T \simeq 1200 \text{ K}$ ) abundance for all quasars at a given equivalent width and blueshift. Quasars with the most extreme outflow signatures are predominantly hot-dust rich. Only bins containing a minimum of two objects are plotted. Change hot dust abundance. 24
- Figure 1.16 25

## LIST OF TABLES

---

|           |                      |    |
|-----------|----------------------|----|
| Table 1.1 | Available photometry | 3  |
| Table 1.2 | Model parameters.    | 13 |

## LISTINGS

---

## ACRONYMS

---

|                 |                              |
|-----------------|------------------------------|
| AGN             | active galactic nuclei       |
| EV <sub>1</sub> | eigenvector 1                |
| SDSS            | Sloan Digital Sky Survey     |
| UV              | ultra-violet                 |
| BH              | black hole                   |
| SED             | spectral energy distribution |
| IR              | infra-red                    |

## SED PROPERTIES

---

### 1.1 INTRODUCTION

AGN emit strongly over many decades in frequency (Figure 1.1). At different frequencies, the emission originates from processes occurring in different regions of the active galactic nuclei (AGN). Hard X-ray emission is dominated by Compton up-scattering of accretion disk photons by electrons in a hot corona (e.g. Sunyaev and Titarchuk, 1980), ultra-violet (UV)/optical by thermal accretion disc emission, infra-red (IR) by dust at a wide range of temperatures, and radio by synchrotron emission in relativistic jets.

Significant diversity is observed in the spectral energy distribution (SED)s of individual objects. However, the systematic study of the dependence of the SED shape on physical parameters has, until very recently, been limited by the difficulty in obtaining a large sample of quasars with good multi-wavelength coverage and large dynamic range in luminosity and redshift. However, we are able to take advantage of a number of recent, sensitive, wide-field photometric surveys, including SDSS (in the UV/optical), UKIDSS (in the near-infrared) and WISE (in the mid-infrared). We will combine this information with the black hole (BH) mass and mass-normalised accretion rate estimates and outflow diagnostics which we developed in Chapters ?? and ?. We will determine whether there are SED-related systematics as a function of outflow signatures and BH mass or Eddington ratio.

Since the physical processes that power AGN are generally understood only qualitatively, almost all AGN SED templates are empirical. The empirical template of Elvis et al., (1994) is still the most commonly cited, despite many additions and updates (e.g. Polletta et al., 2000; Kuraszkiewicz et al., 2003; Risaliti and Elvis, 2004; Richards et al., 2006; Polletta et al., 2007; Lusso et al., 2010; Shang et al., 2011; Marchese et al., 2012; Trichas et al., 2012). However, these composite spectra are often constructed from quasars with a huge range in luminosity as a function of wavelength. In addition, the presence of significant host galaxy at optical wavelengths in low-redshift objects is an additional complication which has not always been taken care of adequately. There is therefore a strong rationale for taking a parametric approach to modelling quasar SEDs. This is the approach we take in this chapter. We then investigate whether the systematic dependence of the model parameters on quasar properties including the BH mass, luminosity, accretion rate and outflow diagnostics.

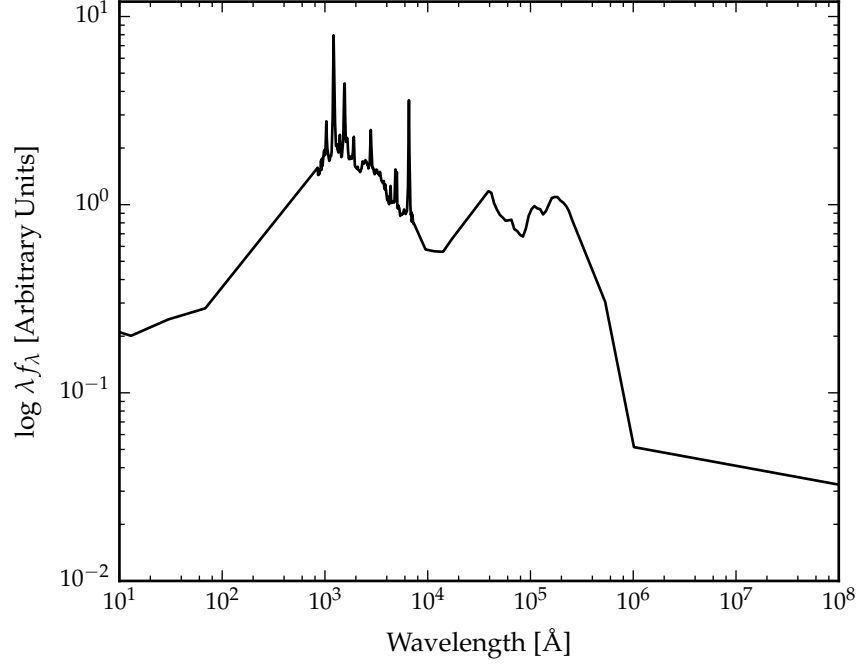


Figure 1.1: Median radio-loud SED from Shang et al., (2011).

## 1.2 DATA

### 1.2.1 SDSS DR7

We use the Seventh Data Release (DR7) of the Sloan Digital Sky Survey (SDSS) spectroscopic quasar catalogue (Schneider et al., 2010), which includes 105,783 objects across 9380 deg<sup>2</sup>. The SDSS obtained images in five broad optical pass-bands: u, g, r, i and z (Table 1.1). We use BEST point-spread function (PSF) magnitudes, correcting for Galactic extinction using the maps of Schlegel, Finkbeiner, and Davis, (1998), assuming a Milky Way (MW) extinction curve (Pei, 1992) and an extinction to reddening ratio  $A(V)/E(B - V) = 3.1$ . Although the SDSS asinh magnitude system is intended to be on the AB system (Oke and Gunn, 1983), the photometric zero-points are known to be slightly off the AB standard. To account for this we add 0.03 mag to the u, g, r and i magnitudes, and 0.05 mag to the z magnitude.

*Where did these numbers come from?*

### 1.2.2 UKIDSS Large Area Survey

We use the ninth data release (DR9) of the UKIRT Infrared Deep Sky Survey (UKIDSS; Lawrence et al., 2007) Large Area Survey (ULAS) which has observed  $\sim 3,200$  deg<sup>2</sup> in four near-IR pass-bands: Y, J, H and K. The ULAS magnitudes are aperture corrected magnitudes in

| Survey | Band | $\lambda_{\text{eff}}$ [ $\mu\text{m}$ ] |
|--------|------|--|
| SDSS   | u    | 0.3543                                   |
|        | g    | 0.4770                                   |
|        | r    | 0.6231                                   |
|        | i    | 0.7625                                   |
|        | z    | 0.9134                                   |
| UKIDSS | Y    | 1.0305                                   |
|        | J    | 1.2483                                   |
|        | H    | 1.6313                                   |
|        | K    | 2.2010                                   |
| WISE   | W1   | 3.4                                      |
|        | W2   | 4.6                                      |
|        | W3   | 12.0                                     |
|        | W4   | 22.0                                     |

Table 1.1: Available photometry

a  $2''$  diameter aperture and are also corrected for Galactic extinction using the Schlegel, Finkbeiner, and Davis, (1998) map.

### 1.2.3 WISE All-WISE Survey

The Wide-field Infrared Explorer (WISE; Wright et al., 2010) mapped almost the entire sky in four mid-IR band-passes: W1, W2, W3 and W4. The WISE AllWISE Data Release ('AllWISE') combines data from the nine month cryogenic phase of the mission that led to the 'AllSky' data release with data from the NEOWISE program (Mainzer et al., 2011). WISE magnitudes are given in the Vega system, and Vega to AB conversion factors are given in the WISE Explanatory Supplement (Cutri et al., 2013).

### 1.2.4 Quasar sample

We include only the 63,855 quasars with i band magnitudes brighter than 19.1, i.e. the quasars selected by the main SDSS quasar selection algorithm for quasars with colours consistent with being at redshifts  $z < 3$  (Richards et al., 2002). Cross-matching (with a  $2''$  radius and picking only the nearest neighbour) the SDSS DR7Q catalogue with the ULAS catalogue, which covers only  $\sim 38\%$  of the SDSS foot-print, resulted in 20,954 matches. Cross-matching to WISE resulted in 20,665 objects detected in one or more of the WISE band-passes. We exclude quasars flagged as broad absorption line (BAL) quasars by Allen et al., (2011) from the sample (leaving 19,853 quasars). The redshift and luminosity distribution of this sample is shown in Figure 1.2.

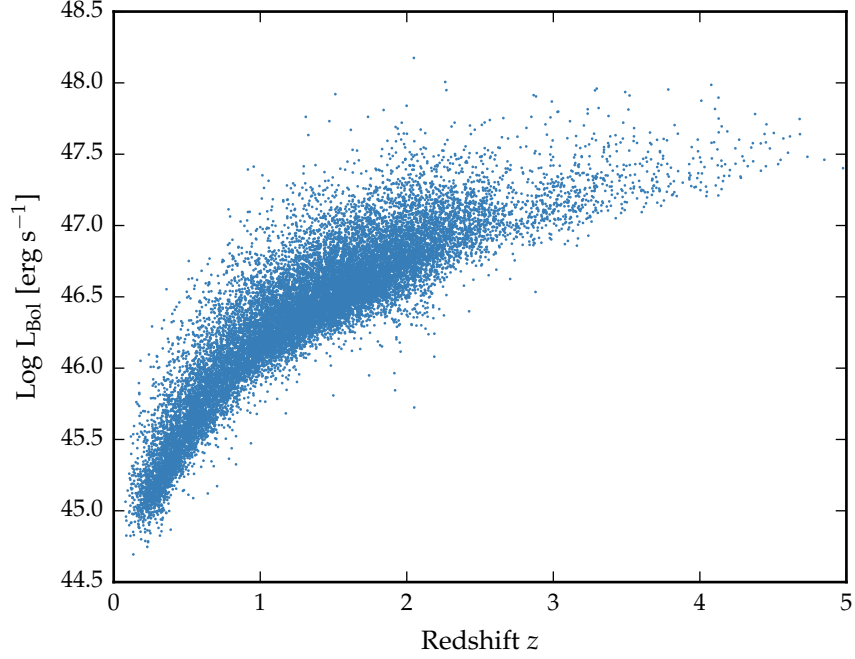


Figure 1.2: Distribution of our sample in the redshift-luminosity plane.

For a given  $i$  magnitude, a quasar with a blue spectrum is more likely to be undetected at longer wavelengths than a quasar with a red spectrum. Therefore, as we allow fainter quasars in to our sample we will be biased towards objects with redder spectra. We verified that above the  $i = 19.1$  limit the sample is 95% complete in all band-passes with  $S/N > 5$  (excluding WISE W3 and W4) and that this fraction is not changing rapidly with the brightness of the sample.

### 1.3 QUASAR SED

We have 19,853 quasars with photometric data from SDSS, UKIDSS and WISE. Our quasars cover the redshift range  $0.2 < z < 4$ , and so this data covers the rest-frame wavelength range from  $800\text{\AA}$  to  $3.8\mu\text{m}$ . In this region the SED is dominated by the accretion disc, emission lines and thermal emission from the hottest ( $T \sim 1200\text{K}$ ) dust. Host galaxy emission is also significant for quasars at redshifts  $z \lesssim 1$ , and the effect of dust extinction at the AGN redshift is another factor which must be considered. In this section, we describe how we have modelled emission from these different physical processes. The model spectrum is shown in Figure 1.3, with each of the main components indicated.



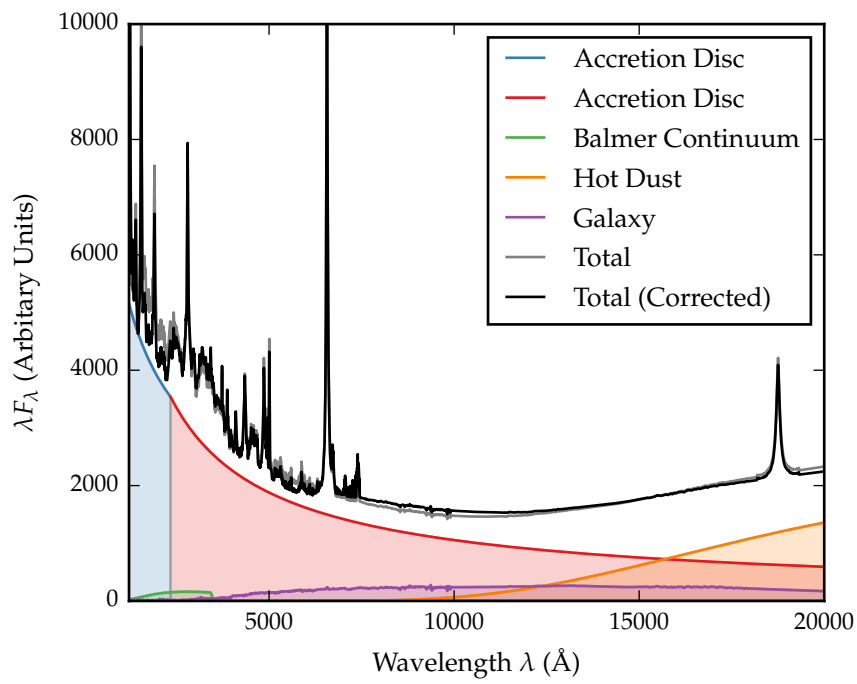


Figure 1.3: Model spectrum at  $z = 1$ , showing the contributions to the total flux from the blue power-law slope, red power-law slope, Balmer continuum, blackbody, emission line spectrum and host galaxy

#### 1.4 SED MODEL

##### 1.4.1 Accretion Disc

Thermal accretion disc emission in the 0.1 - 1  $\mu\text{m}$  region is characterised by a broken power-law with three free parameters: a break-wavelength  $\lambda_{\text{break}}$ , a blue power-law index  $\alpha_{\text{blue}}$  for wavelengths shorter than the break wavelength, and a red power-law index  $\alpha_{\text{red}}$  for wavelengths longer than the break wavelength.

##### 1.4.2 Balmer Continuum

High order Balmer lines, optically thin Balmer continuum emission, two-photon emission and Fe II emission blend together to form a distinct feature in quasar spectra at  $\sim 3000\text{\AA}$ . We simulate the Balmer continuum we use the empirical model given by Grandi, (1982):

$$F(\lambda) = C_{\text{BC}} \times B_{\lambda}(T_e)(1 - e^{-\tau_{\lambda}}); \quad \lambda \leq \lambda_{\text{BE}} \quad (1.1)$$

where  $C_{\text{BC}}$  is a normalisation factor,  $B_{\lambda}(T_e)$  is the Planck function,  $T_e = 13150\text{K}$  is the effective temperature,  $\lambda_{\text{BE}} = 3460\text{\AA}$  is the wavelength at the Balmer edge, and  $\tau_{\lambda} = \tau_{\text{BE}} (\lambda_{\text{BE}}/\lambda)^{-3}$  is the optical depth with  $\tau_{\text{BE}} = 45$  the optical depth at  $\lambda_{\text{BE}}$ . This function is convolved with a Gaussian with  $\sigma = 5000\text{km s}^{-1}$  to simulate the effect of bulk velocity shifts comparable to those present in broad AGN emission lines.

##### 1.4.3 Hot Dust

Thermal emission from hot dust, which dominates the SED at wavelengths longer than  $1\mu\text{m}$ , is modeled using a simple blackbody

$$F_{\lambda} = C_{\text{BB}} \times \frac{2hc^2}{\lambda^5} \frac{1}{e^{\frac{hc}{\lambda k_B T_{\text{BB}}}} - 1}, \quad (1.2)$$

with two free parameters: the temperature  $T_{\text{BB}}$  and normalisation.

##### 1.4.4 Emission Lines

We use an emission line template taken from Francis et al., (1991), which has been extended by Maddox and Hewett, (2006) to include the  $\text{H}\alpha$  and  $\text{Pa}\alpha$  emission lines. All emission lines, with the exception of  $\text{H}\alpha$ , are scaled using a single free parameter  $C_{\text{EL}}$ , which preserves relative equivalent widths:

$$F_{\lambda} = C_{\text{EL}} \times \frac{F_{\lambda,\text{el}}}{F_{\lambda,\text{cont}}} \times F_{\lambda}; \quad \lambda < 4700\text{\AA} \text{ and } \lambda > 7000\text{\AA} \quad (1.3)$$

where  $F_{\lambda,\text{el}}$  is the emission line template,  $F_{\lambda,\text{cont}}$  is the continuum flux in the template, and  $F_{\lambda}$  is the continuum flux in the SED model.  $\text{H}\alpha$ , one of the strongest broad emission lines, is scaled separately:

$$F_{\lambda} = C_{\text{EL}} \times C_{\text{H}\alpha} \times \left( \frac{L(z)}{L(z_{\text{nrn}})} \right)^{-\beta} \times \frac{F_{\lambda,\text{el}}}{F_{\lambda,\text{cont}}} \times F_{\lambda}; \quad 4700\text{\AA} < \lambda < 7000\text{\AA} \quad (1.4)$$

The luminosity dependence of the  $\text{H}\alpha$  EQW (i.e. the Baldwin effect) is parametrised with a simple power-law with slope  $\beta = 0.04$ . The redshift dependence of the mean AGN luminosity  $L(z)$  for the SDSS quasar catalogue has been determined empirically.

#### 1.4.5 Host Galaxy

Emission from the host galaxy is important for AGN at redshifts  $z \lesssim 1$ , particularly in the region around the  $1\mu\text{m}$  inflection point in the quasar SED. We use a  $z = 0$  Sb template from Mannucci et al., (2001), which does not evolve with redshift. The template is scaled by a multiplicative factor  $C_{\text{Gal}}$  and added to the AGN SED. We define a new parameter,  $\eta$ , the fractional contribution from the host galaxy to the total flux in the interval 4000 and 5000 $\text{\AA}$ :

$$\eta \equiv \frac{C_{\text{Gal}} F_{\text{Gal}}}{F_{\text{AGN}} + C_{\text{Gal}} F_{\text{Gal}}}, \quad (1.5)$$

where  $F_{\text{Gal}}$  and  $F_{\text{AGN}}$  are the flux of the galaxy and AGN respectively. Rearranging for the scaling factor  $C_{\text{Gal}}$  gives:

$$C_{\text{Gal}} = \frac{\eta}{1 - \eta} \frac{F_{\text{AGN}}}{F_{\text{Gal}}}. \quad (1.6)$$

The fractional contribution to the total emission from the host galaxy changes as a function of the AGN luminosity and, in a flux-limited sample, the mean AGN luminosity increases as the redshift increases. We parametrize the AGN luminosity dependence of the host galaxy luminosity as a power-law:

$$\frac{L_{\text{Gal}}}{L_{\text{AGN}}} = L_{\text{AGN}}^{\beta-1} \quad (1.7)$$

with slope  $\beta = 0.42$  (Maddox and Hewett, 2006). The galaxy scaling factor  $C_{\text{Gal}}$  becomes

$$C_{\text{Gal}} = \frac{\eta}{1 - \eta} \frac{F_{\text{AGN}}}{F_{\text{Gal}}} \left[ \frac{L_{\text{Gal}}(z)}{L_{\text{AGN}}(z)} \right] \left[ \frac{L_{\text{Gal}}(z_{\text{nrn}})}{L_{\text{AGN}}(z_{\text{nrn}})} \right]^{-1} \quad (1.8)$$

$$= \frac{\eta}{1 - \eta} \frac{F_{\text{AGN}}}{F_{\text{Gal}}} \left[ \frac{L_{\text{AGN}}(z)}{L_{\text{AGN}}(z_{\text{nrn}})} \right]^{\beta-1}, \quad (1.9)$$

where  $z_{\text{nrn}}$  is an arbitrary redshift at which the fractional contribution from the host galaxy is by definition  $\eta$ .

#### 1.4.6 Dust Extinction

The selection criteria of the SDSS DR7Q catalogue are sensitive to quasars with moderate amounts of dust reddening (possibly as high as  $E(B - V) \sim 0.5$ ; Richards et al., 2003) at the redshift of the quasar, and so we included the effect of dust extinction in our model. We use an extinction curve appropriate for the quasar population which has been derived by Paul Hewett. To derive the quasar extinction curve, UKIDSS photometry was used to provide an  $E(B - V)$  estimate, via the magnitude displacement of each quasar from the locus of un-reddened objects. At redshifts  $2 < z < 3$  the reddening measure is made at rest-frame wavelengths 3500-7000Å, where Galaxy, LMC and SMC extinction curves are very similar. The SDSS spectra of the same objects are then employed to generate an empirical extinction curve in the ultraviolet, down to 1200Å. The resulting curve has no 2200Å feature and rises rapidly with decreasing wavelength but is not as steep as the SMC curve. The extinctions curves give the colour excess  $E(B - \lambda)$  relative to the colour excess  $E(B - V)$  as a function of wavelength  $\lambda$ . The colour excess  $E(B - V)$  is related to the extinction in the V band,  $A(V)$ , via a parameter  $R$ ,

$$A(V) = R \times E(B - V) \quad (1.10)$$

where  $R = 3$ . Hence the extinction at a wavelength  $\lambda$   $A(\lambda)$  is

$$A(\lambda) = E(B - V) \times \left[ \frac{E(\lambda - V)}{E(B - V)} + R \right] \quad (1.11)$$

where the colour excess  $E(B - V)$  is a free parameter in our model. The attenuation of the flux at a given wavelength is then:

$$F_\lambda = F_\lambda 10^{-A(\lambda)/2.5} \quad (1.12)$$

in the rest frame of the quasar.

### 1.5 THE 'STANDARD' SED MODEL

- Given the same parameters, my model and Paul's look identical
- I'm generating model colours using my model and Paul's best-fit parameters, and Paul's correction

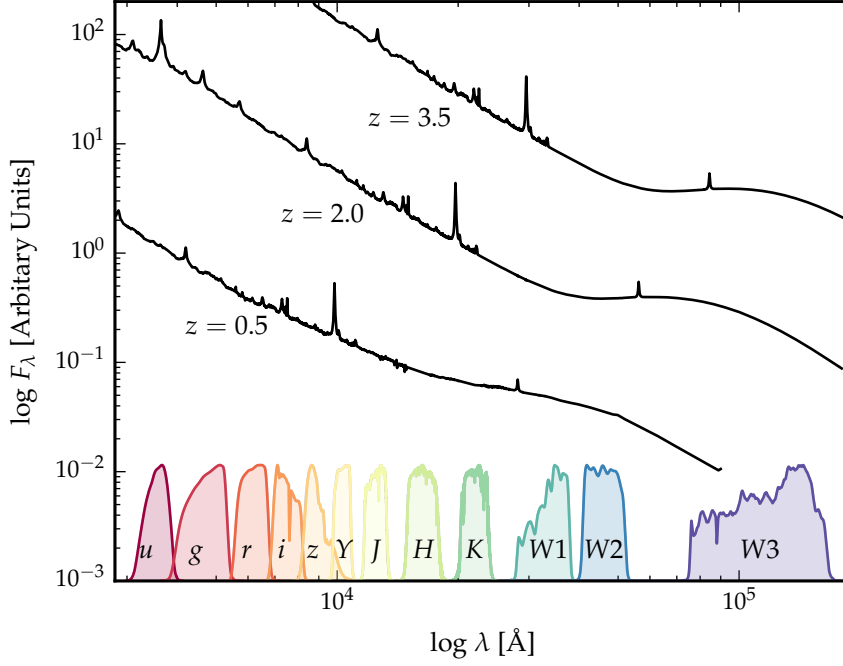


Figure 1.4: Model spectrum at three different redshifts (each arbitrarily scaled), and throughput functions for SDSS, UKIDSS and WISE band-passes.

- Do my model colours look the same as Paul's? (i.e. is there a bug in my code?)
- Can I generate the same median colours as Paul? (i.e. what sample is being used? what magnitudes?)
- Can I do my own fit to the data?

We will begin by deriving a 'standard' SED model by constraining a single set of parameters with our sample of 19,853 quasars, encompassing a range of redshifts, luminosities, accretion rates etc. The free parameters in our model are the blue power-law slope, the red power-law slope, the power-law break wavelength, the blackbody temperature, the blackbody normalisation, the emission line equivalent width scaling, the  $H\alpha$  scaling and the fractional contribution from the host galaxy to the total flux. The reddening  $E(B - V)$  is fixed to zero, since a large fraction of SDSS quasars have very small amounts of dust reddening (Richards et al., 2003). We generate a set of model observed spectra at redshifts from  $z = 0.25$  to  $z = 3.75$  in intervals of  $\Delta z = 0.1$ . The SED model is shown at three different redshifts in Figure 1.4. The magnitude of the model is given by

$$m_\lambda(P) = -2.5 \log(f_\lambda(P)) - m_0(P), \quad (1.13)$$

where  $m_0(P)$  is the zero-point magnitude of band  $P$  and the mean flux density  $f_\lambda(P)$  is given by

$$f_\lambda(P) = \frac{\int P(\lambda) f_\lambda(\lambda) \lambda d\lambda}{\int P(\lambda) \lambda d\lambda} \quad (1.14)$$

where  $P(\lambda)$  is the dimensionless throughput function of the band-pass. Magnitudes are calculated in the AB system, in which case the zero-point flux per unit wavelength is

$$\frac{f_\lambda(\lambda)}{\text{erg cm}^{-2} \text{ s}^{-1} \text{ \AA}^{-1}} = 0.1087 \left( \frac{\lambda}{\text{\AA}} \right)^{-2}. \quad (1.15)$$

We divide our quasar sample into the same redshift bins. In each bin we normalise the quasar SEDs in the SDSS  $i$  band, and then calculate the median SED. The model SED in each redshift bin is similarly normalised. The chi-squared statistic is then minimised using the ‘nelder-mead’ algorithm.

Our SED model is valid only up to  $\lambda \sim 3\mu\text{m}$  in the quasar rest frame (the approximate wavelength of the peak in hot dust emission); beyond this additional contributions to the total flux from cooler dust will become significant. This prevents us from using the two highest wavelength WISE bands in the fit. We also exclude the SDSS  $u$  and  $g$  band-passes from the fit at  $z > 2.7$  and  $z > 3.7$  respectively, where these bands start to be affected by Lyman $\alpha$  forest absorption.

## 1.6 RESULTS

*Re-do fit*

*Need to show individual quasars.*

The best-fitting parameters from the fit are shown in Table 1.2. The colours ( $u - g$ ,  $g - r$ , etc.) of the median SED, the individual quasars, and the best-fitting model are plotted as a function of redshift in Figs. 1.5 and 1.6. Most of the large variations that can be seen in the median colours of the quasars as a function of redshift are due to strong emission lines being redshifted in to and out of the band-passes of the band-passes being used.

## 1.7 DISCUSSION OF FIT

In Figure 1.7 we show the difference between the magnitudes from the best-fitting model and the median magnitudes from the sample. We have transformed the effective wavelengths of the band-passes to the rest frame of the quasars in each redshift bin, to give to the residuals as a function of rest-frame wavelength. We represent the residuals measured in each band-pass using a different coloured line. Differences between residuals from different band-passes at the same

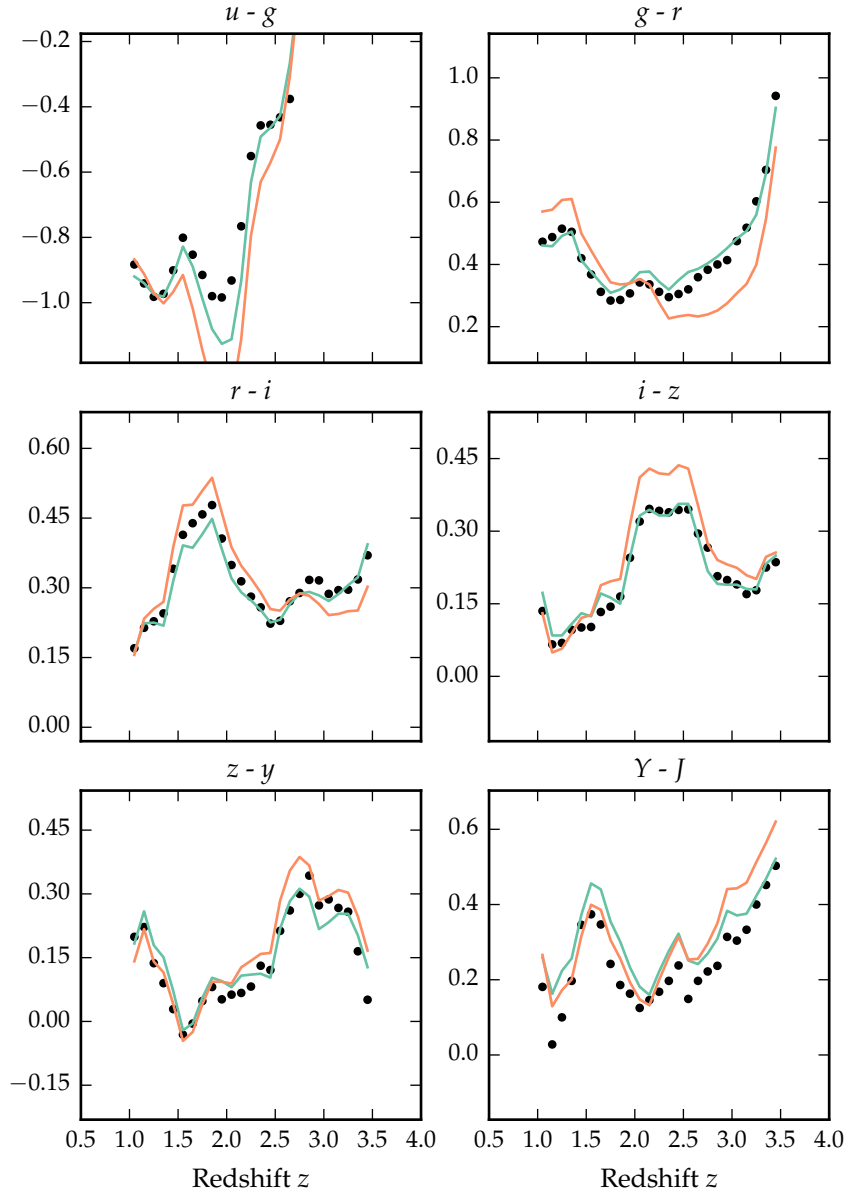


Figure 1.5: Colours of median SED and best-fitting model, with and without correction. Corrected is in orange, uncorrected in green. Check with Paul. Correction often makes colours a lot worse. Once got to the bottom of this just show with correction.

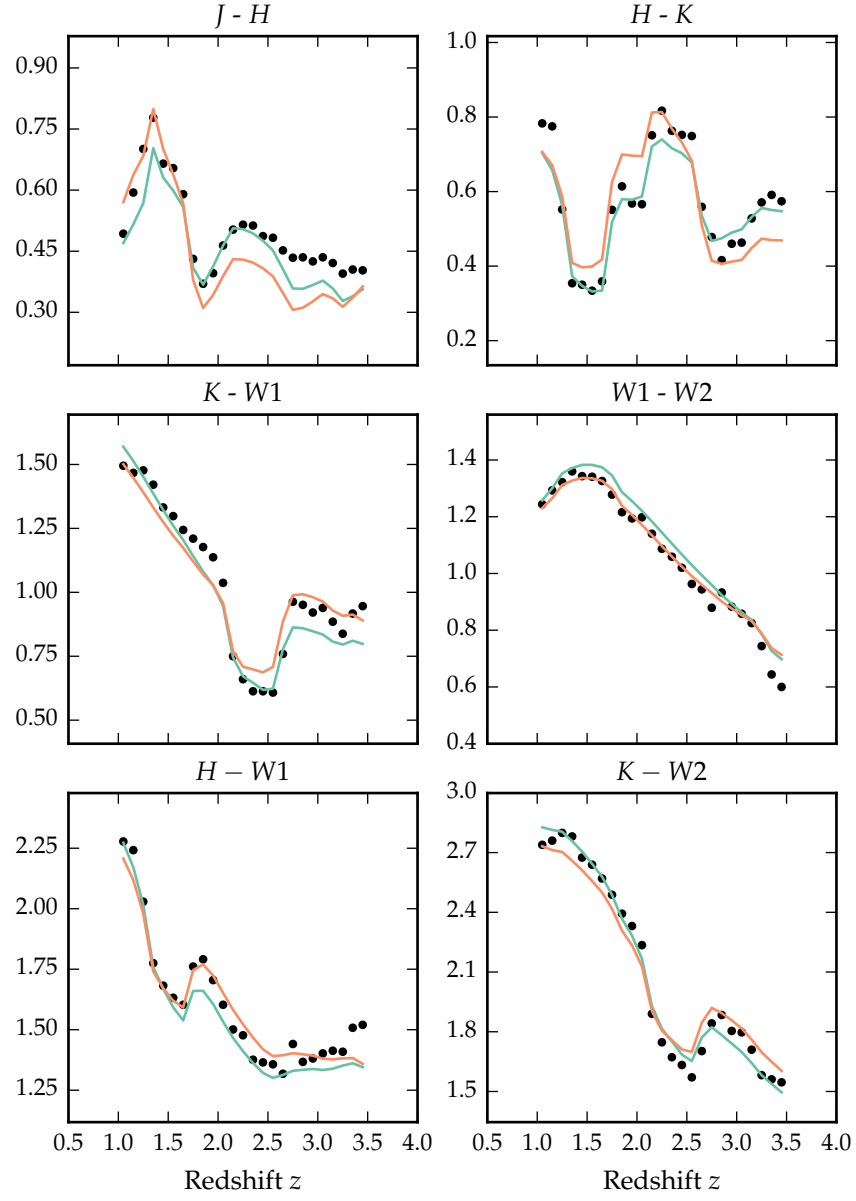
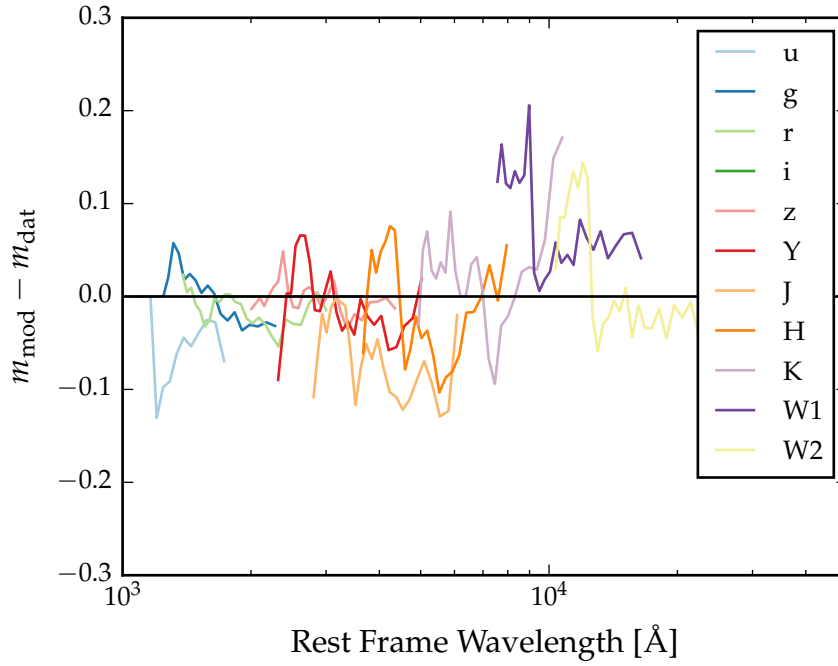


Figure 1.6: Colours of median SED (black circles), individual objects (grey points), best-fitting model (black line) as a function of redshift.



| Parameter                        | Symbol                   | Value  |
|----------------------------------|--------------------------|--------|
| Blue power-law index             | $\alpha_{\text{blue}}$   | 0.58   |
| Red power-law index              | $\alpha_{\text{red}}$    | -0.04  |
| Power-law break                  | $\lambda_{\text{break}}$ | 2945   |
| Blackbody temperature            | $T_{\text{BB}}$          | 1216 K |
| Blackbody normalisation          | $C_{\text{BB}}$          | 0.22   |
| Emission line scaling            | $C_{\text{EL}}$          | 0.63   |
| H $\alpha$ emission line scaling | $C_{\text{EL}}$          | 0.63   |
| Galaxy fraction                  | $\eta$                   | 0.29   |
| E(B-V)                           | E(B-V)                   | 0.00   |

Table 1.2: Model parameters.

Figure 1.7: Residuals from fit as a function of rest-frame wavelength. [Show before and after correction.](#)

rest-frame wavelength could indicate redshift evolution of the typical quasar SED.

The residuals indicate that over a large redshift range the model does a fairly good at reproducing the median observed colours of the sample. Most discrepancies are at the  $< 0.1$  mag level. It is remarkable that a single model is so effective; the properties of a typical quasar to not change significantly over a wide range of redshifts and luminosities. Many authors have found no significant dependence of the mean SED on properties such as redshift, bolometric luminosity, BH mass, or accretion rate (e.g. Elvis et al., 2012; Hao et al., 2013). On the other hand, for the individual objects there is a significant scatter about the mean. In general, our goal is to use this intrinsic spread in SED properties in order to understand the diversity in physical quasar properties.

*Need individual points on plot to show this.*

#### 1.7.1 Flux Correction

The most noticeable feature in Figure 1.7 is a bump around  $1\mu\text{m}$ , where the model underestimates the flux of the population by  $\sim 0.1$  mag. If the model is a poor fit to the data, it can produce strong redshift-dependent systematics. A blackbody component with a higher temperature would contribute more flux in this region, which could potentially lead to redshift-dependent systematic errors. To avoid this we derived a correction to our model which accounted for the  $1\mu\text{m}$  flux discrepancy.

*Describe Paul's empirical correction.*

### 1.8 HOT DUST

Including a black-body with  $T \sim 1250\text{K}$ , a simple parametric model matches the ugrizYJHKW<sub>1</sub>W<sub>2</sub> (SDSS+UKIDSS+WISE) median colours of luminous quasars at redshifts  $0.2 < z < 0.4$ . The spread in the KW<sub>1</sub>W<sub>2</sub> colours (Figure 1.10), probing the rest-frame  $\sim 1\text{-}2$  micron region, is significant and strongly suggests presence of real variation in the "hot dust" temperature and luminosity among the quasars.

#### 1.8.1 Parametrising the hot dust emission

We characterise the hot dust properties of our sample in terms of the temperature and luminosity of a blackbody. We choose to parametrise the luminosity in terms of the NIR to UV luminosity ratio (which is proportional to the covering factor of hot dust ( $L_{\text{NIR}}/L_{\text{Bol}}$ ) used in other studies (Roseboom et al., 2013). The UV and NIR luminosity are calculated between 2000 and 9000Å and 1 and 3  $\mu\text{m}$  respectively.

In Figure 1.8 we see that the two parameters are clearly correlated. For a lower temperature black-body the NIR to UV luminosity ratio is larger. Such a correlation is to be expected: as the black-body tem-

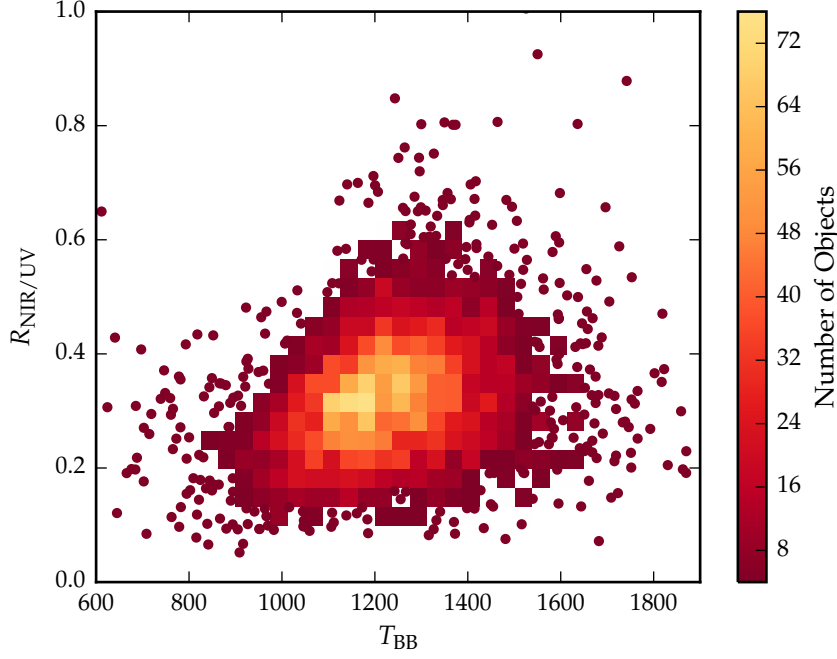


Figure 1.8: Ratio of NIR to UV luminosity ( $R_{\text{NIR/UV}}$ ) against temperature ( $T_{\text{BB}}$ ) for low- $z$  sample. The density of points is shown in more dense regions of the space, and individual objects in less dense regions.

perature is lowered, the peak shifts to longer-wavelengths (following Wien’s displacement law). Because of this degeneracy we need to be very careful to separate out real trends of  $R_{\text{NIR/UV}}$  with other quasar properties from indirect trends resulting from a mutual dependence on  $T_{\text{BB}}$ .

Some previous studies (e.g. Wang et al., 2013; Zhang et al., 2014) have instead parametrised the near-IR emission using a power-law ( $\propto \lambda^{\beta_{\text{NIR}}}$ ), with  $\beta \simeq 0.5$ . We tested this parametrisation, and evaluated it’s effectiveness relative to using a black-body. The power-law is normalised at 9000Å, where its flux is set equal to the flux of the UV/optical model. The NIR power-law slope is fit between  $\sim 1$  and  $2.4\mu\text{m}$  (with the exact wavelength region being fit depending on the redshift of the quasar). We found large residuals in the best-fitting model which varied systematically as a function of  $\lambda_{\text{eff}}/(1+z)$ . This suggests that the power-law model is a poor fit to the shape of the near-IR emission. One needs to take care in looking at trends with luminosity given the observed-frame passband information on the rest-frame SED can produce some strong systematics with redshift, particularly if the SED-model is not a good fit to the actual SED. A similar conclusion was reached by Gallagher et al.

### 1.8.2 Sample

Our goal is to determine the temperature and abundance of the hot dust component in individual quasars. These properties will be measured by fitting a model to the SDSS-UKIDSS-WISE photometry. Constraining a  $T \sim 1200\text{K}$  blackbody component in the SED model requires photometric data covering  $\sim 1\text{--}3\mu\text{m}$  in the rest-frame of the quasar.

The observed-frame wavelength coverage of the available passbands limits the redshift range of the quasars which can be used. One does need to take care in looking at trends with luminosity given the observed-frame passband information on the rest-frame SED can produce some strong systematics with redshift, particularly if the SED-model is not a good fit to the actual SED. We consider only quasars at redshifts  $z > 1$  where the relative host galaxy contribution to the SED is negligible. At redshifts  $1 \lesssim z \lesssim 1.5$  the available *ugrizYJHKW1W2* photometry provides good coverage of the rest-frame SED up to  $\sim 2\mu\text{m}$ . At  $z \sim 1.5$  the *W2* passband is shifted to  $\sim 1.8\mu\text{m}$ ; at higher redshifts the wavelength coverage of the *W2* band becomes much less than the peak wavelength of a  $T \sim 1200\text{K}$  blackbody and experiments showed that such a component can not be adequately constrained by the available photometry. Quasars in the redshift interval  $1.5 < z < 2$  are therefore excluded from our sample.

For the quasars at  $z \sim 1$  the WISE *W3* band is probing rest-frame wavelengths of  $\sim 5 - 6\mu\text{m}$ . This region of the SED is dominated by emission from cooler, more distant dust, which is not accounted for in our model. However, at redshifts  $z \gtrsim 2$  the WISE *W3* passband probes sufficiently short wavelengths to be useful in constraining the shape of the hot blackbody component. Therefore for quasars at redshifts  $z > 2$  we again have sufficient constraints from the *ugrizYJHKW1W2W3* photometry to determine the temperature and normalisation of the blackbody component. There are few objects in our sample with redshifts  $z > 2.7$ , and so we set this as an upper limit on the redshift of our sample. Because of these constraints, our sample is divided in to two parts: one at low redshifts ( $1 < z < 1.5$ ) and the other at higher redshifts ( $2 < z < 2.7$ ).

We impose a lower-limit signal-to-noise ratio  $(S/N) > 5$  magnitudes in the *K*, *W1* and *W2* band-passes for the low- $z$  sample and  $S/N > 5$  in the *W1*, *W2*, and *W3* band-passes for the high- $z$  sample to ensure reliable photometry. This gives us 5,910 quasars in our low- $z$  sample and 1,989 quasars in our high- $z$  sample.

We will hold most parameters fixed, and vary only those we are interested in, i.e. the blackbody parameters which parametrise the NIR emission. Therefore we need to define a sub-sample of objects which we know are well fit by our standard SED model in the UV/optical region. This means excluding objects with extreme emission line equivalent widths or significant dust extinction. We use the *i* – *K* colours

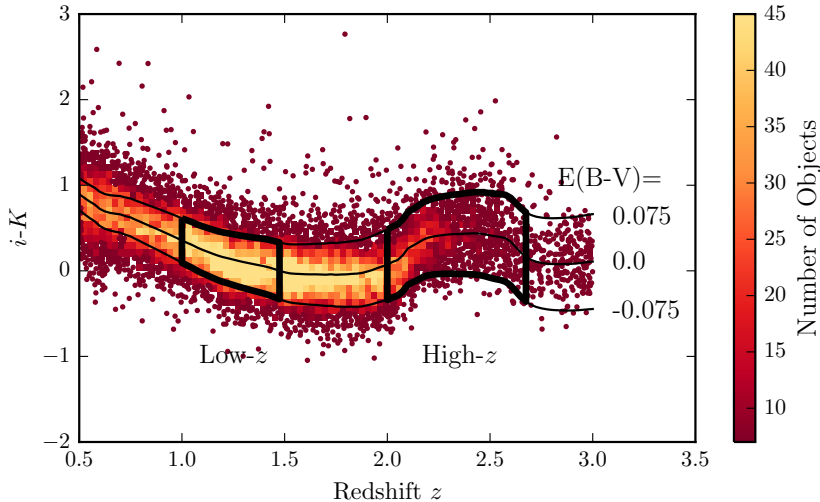


Figure 1.9:  $i - K$  colours of non-BALQSO DR7Q quasars with  $i > 19.1$  as a function of redshift. The lines show the colours of our model with varying amounts of dust extinction. Quasars with extinction  $|E(B - V)| > 0.075$  are excluded.

of the quasars as a measure of the overall colour of the quasars as it provides the longest baseline in wavelength without being affected by absorption in the  $\text{Ly}\alpha$  forest at high redshifts. A significant amount of the scatter in  $i - K$  can be attributed to intrinsic variations in the UV power-law slopes of the individual quasars, which is why we allow a negative reddening. However, there is a clear ‘red tail’ to the colour distribution which can be explained by dust reddening at the redshift of the quasar. We discarded from our sample quasars with  $i - K$  colours redder than our standard model with dust reddening  $E(B-V) = 0.075$  and bluer than  $E(B-V) = -0.075$  (Figure 1.9). Following this cut we are left with 4,615 quasars in our low- $z$  sample and 1,692 quasars in our high- $z$  sample.

### 1.8.3 Diversity in hot dust properties

In Figure 1.10 we plot the  $W1 - W2$  colours of the sample as a function of redshift at  $z < 3$ . In this redshift range the  $W1$  and  $W2$  band-passes are probing the  $1.2 - 2.8\mu\text{m}$  and  $1.6 - 3.8\mu\text{m}$  region of the rest frame SED respectively. For reference, the peak wavelength is at  $2.4\mu\text{m}$  for a black-body radiating at 1200K (close to the sublimation temperature of dust grains). At any given redshift we see a  $\sim 0.5$  mag dispersion in the  $W1 - W2$  colours.

On the same axes in the Figure we have plotted the  $W1 - W2$  colours derived from our SED model with a fixed blackbody temperature (1216K) and a ratio of NIR to UV luminosity ranging from 0.0 to 1.0, with the other model parameters held constant. We con-

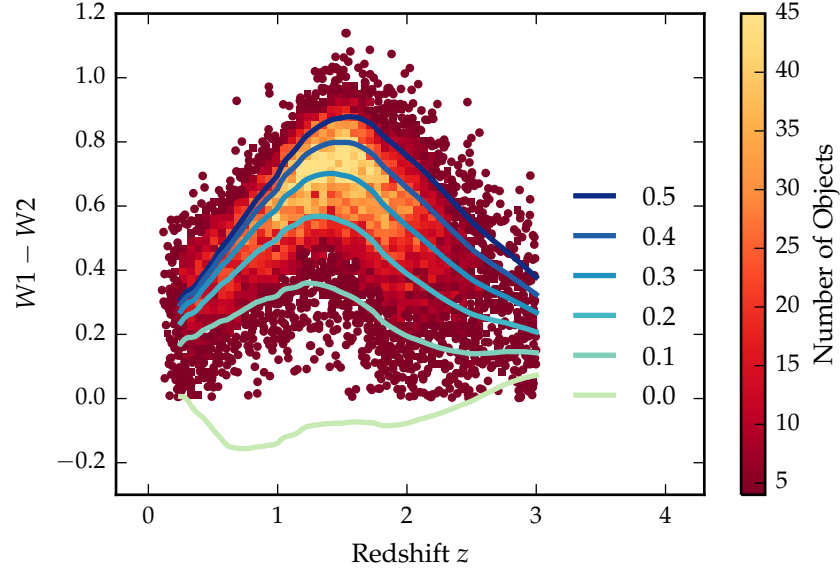


Figure 1.10:  $W1 - W2$  colours of sample as a function of redshift. Above a certain density threshold points are represented by a density plot. On top we plot the colours of our standard SED model, with a fixed temperature and a varying NIR ( $1 - 3 \mu\text{m}$ ) to UV ratio.

clude that even with the sample restricted to be fairly uniform in its UV/optical properties, we still get an interesting spread in  $W1-W2$  colours, which we can use to learn about the diversity of NIR properties in our sample. In the rest of this chapter we will characterise the hot dust properties of our sample, and test its relation to quasar properties such as luminosity, black-hole mass and normalised accretion rate, and outflow-properties.

### 1.9 FITTING PROCEDURE

We will fit a model to the individual quasar SEDs, allowing the temperature and normalisation of the black body component to vary. The model spectrum is redshifted to the redshift of the quasar being fit and is then multiplied by the `ugrizYJHMW1W2W3` throughput functions and normalised appropriately to give AB magnitudes. To fit the model to the data we minimise the sum of the squares of the differences between the elements in the model magnitude array and the elements in the data magnitude array. To avoid significant absorption in the Lyman- $\alpha$  forest at high- $z$ , we restrict our fitting to wavelengths greater than  $2000\text{\AA}$ ; when the effective wavelength of a band-pass falls below this limit the band-pass is excluded from the fit. The minimisation is done using the 'nelder-mead' method, as implemented in the `minimize` function from the Python module `scipy`.

*2000Å is quite large  
given the  
Lyman-alpha forest  
impacts from 1216Å.*

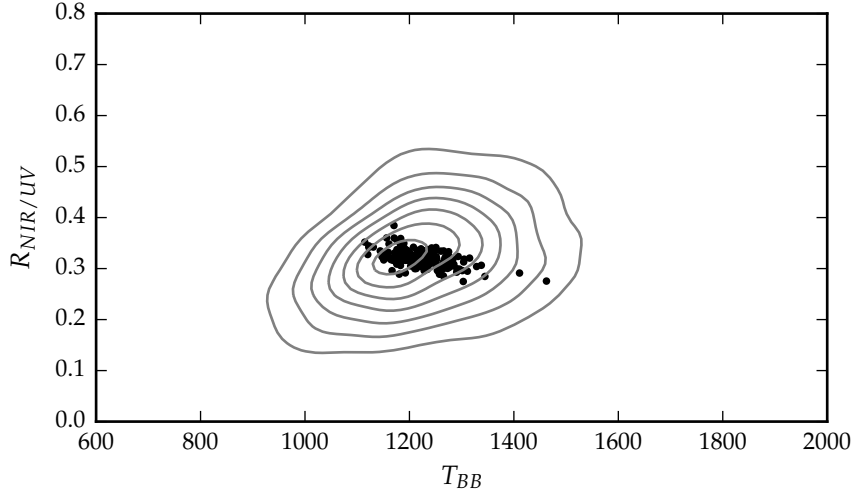


Figure 1.11: Ratio of NIR to UV luminosity ( $R_{\text{NIR/UV}}$ ) against temperature ( $T_{\text{BB}}$ ). The grey contours show equally-spaced lines of constant probability density generated using a Gaussian kernel-density estimator on our data sample. The black points are for our mock data.

## 1.10 RESULTS

In Figure 1.8 we show that there is quite a range of temperature and normalisation present in our sample. However, we need to check how much of this is due simply to uncertainties in the fits stemming from uncertainties in the photometry. In order to achieve this we took our standard SED model with a single temperature and normalisation black-body component, and generated 200 mock SEDs with a brightness distribution similar to that of our real sample. We estimated the mean uncertainty of the magnitudes in the K, W<sub>1</sub>, and W<sub>2</sub> band-passes as a function of apparent brightness. We then sampled the K, W<sub>1</sub>, and W<sub>2</sub> magnitudes from Gaussian distributions, with a mean equal to the magnitude of the model SED, and the width equal to the mean uncertainty at the appropriate brightness. Finally, we fit these mock SEDs using our standard fitting procedure. The results are shown in the Figure below, on top of the results from our real sample (shown as grey contours). We can see that uncertainty in the photometry introduces a significant scatter to the temperature, but that this scatter is less than the intrinsic scatter in the data. This demonstrates that there is a real distribution of hot dust temperatures and luminosities in our sample.

*Basic results.  
Histogram  
parameters, show  
degeneracy  
Show some example  
fits? Show overlayed  
data/model with  
alpha=0.1?*

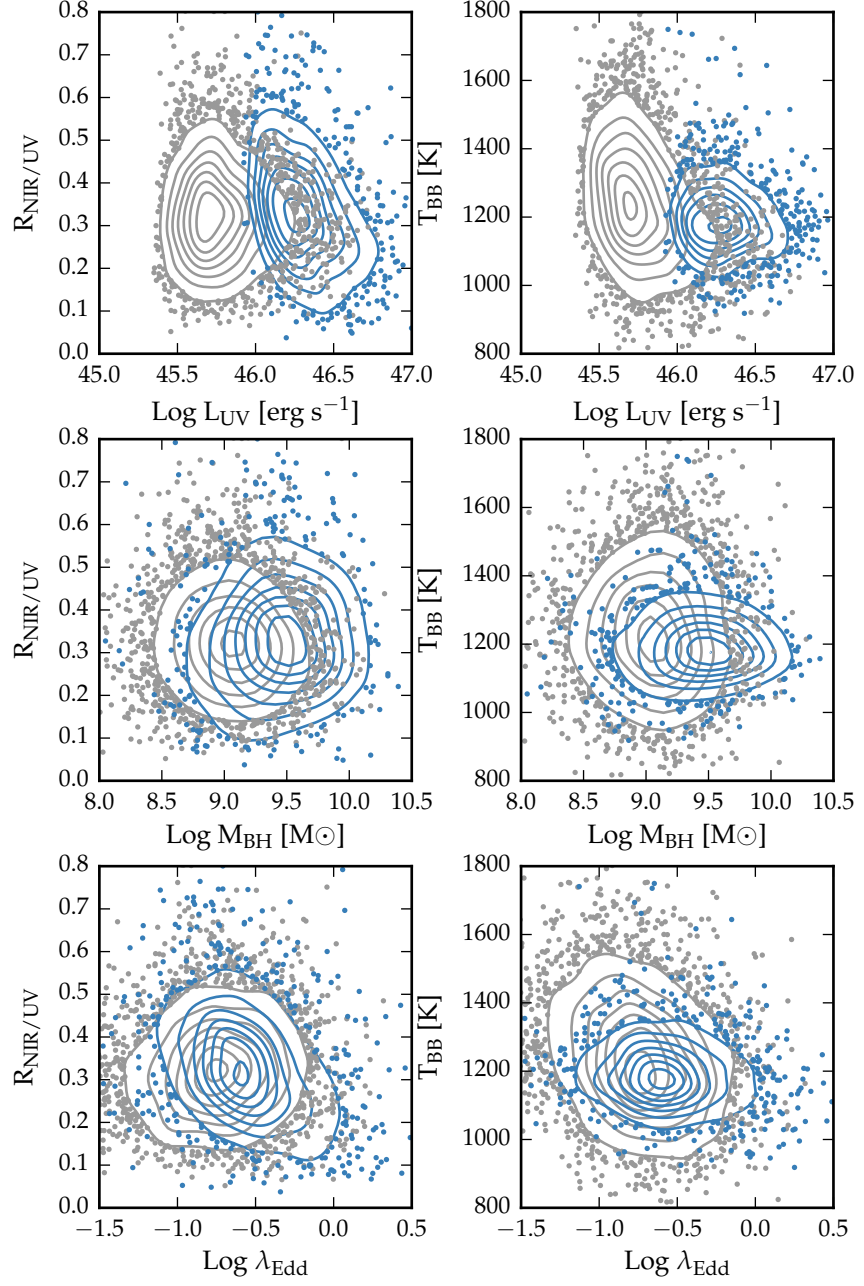


Figure 1.12: Best-fit black-body temperature against UV luminosity (left), black-hole mass (centre) and Eddington ratio (right) for  $1 < z < 1.5$  sample (black) and  $2 < z < 2.7$  sample (black). In region of high-density we represent the density with contours generated using a Gaussian kernel density estimation. **Needs re-making with new BH masses.**



### 1.10.1 Correlations with quasar properties

We now look for correlations between the properties of the black-bodies we have fitted to the hot dust emission and other properties of the quasar such as redshift, black-hole mass, and normalised accretion rate (Eddington ratio).

*Calculate new BH masses and redo this section.*

### 1.10.2 Spectral properties

In the dusty wind model - first proposed by Konigl and Kartje, (1994) and later developed by, amongst others, Everett, (2005), Elitzur and Shlosman, (2006), Keating et al., (2012) - the 'torus' is the dusty part of a magneto-hydrodynamic wind beyond the dust sublimation radius. The MHD wind is roughly polar, and so the hot dust forms a vertical 'wall' around the accretion disc. UV photons from the accretion disc accelerate the wind via radiation line driving. That flattens the geometry of the wind and exposes more surface area that is viewable on a relatively face-on line of sight. The radiation pressure is increased at higher luminosities and/or accretion rates. This can flatten the geometry of the wind, thereby increasing the range of angles for which the inner edge of the dusty wind - where dust is at its sublimation temperature - can be observed. A direct prediction is therefore that the in a quasars with high accretion rates and strong outflows, the emission from hot dust should be enhanced.

#### 1.10.2.1 Composite spectra

Is there a connection between the hot dust properties and EV1? To test this we can divide the quasar sample by hot dust properties, and then generate composite spectra. The eigenvector 1 (EV1) original EV1 correlates - Fe II, H $\beta$ , [O III] - are at around 4000-6000Å. The SDSS spectra are probing shorter wavelengths at redshifts  $z \gtrsim 1$ . Recall that our sample does not include any quasars at redshifts  $z < 1$ , where the host galaxy emission starts to become significant.

The  $z < 0.8$  SDSS spectrum composite comparison for the small and large  $\beta_{\text{NIR}}$  sub-samples (Figure ??) is a very direct illustration of EV1. Hot dust emission increases with Fe II EW. We also note that the amount of hot dust correlates with the Si III/C III] emission ratios. The Si III/C III] ratio is generally considered to be a good indicator of density and is one of the primary EV1 correlates. The relative flux ratio of Si III to C III] increases when C IV is more blue-shifted (Richards et al., 2011). The Mg II emission line has exactly the same profile/shape for the two samples (apparent changes in Mg II seen in Fig. 1.13 are the result of changes in Fe II at wavelengths just shortward of the line). Finally, we note that objects with more hot dust are slightly redder.

*Need to decide what to do here. If I say host galaxy is significant using the power-law slope won't help. Use blackbody fits instead?*

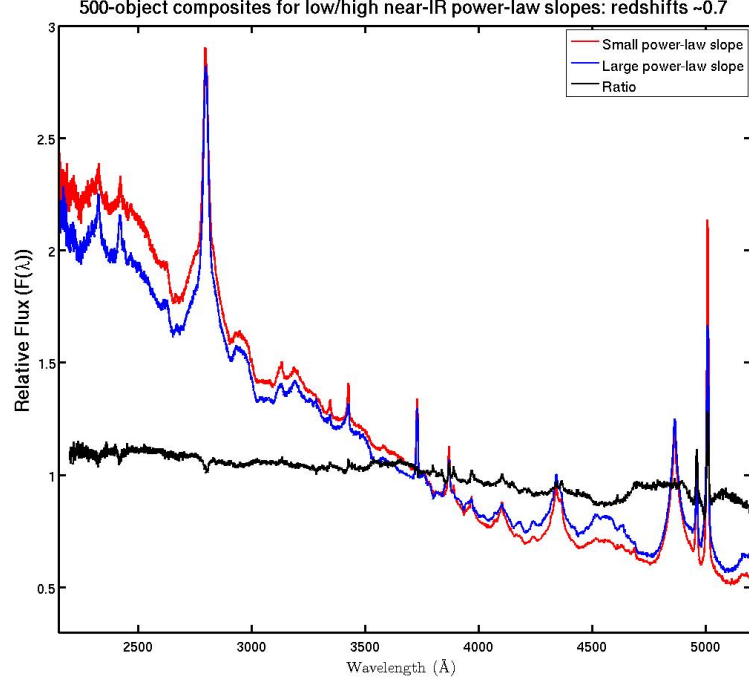


Figure 1.13: Composite SDSS spectra for objects at  $z \sim 0.7$ . We have divided sample into objects with objects best-fit by small (red line) and large (red line) values of  $\beta$ . **Remake if possible.**

Shen and Ho, (2014) also find that torus emission is enhanced in quasars with larger  $R_{\text{FeII}}$ . They suggests that this may be caused by more efficient disc winds that facilitate the formation of a dusty torus.

#### 1.10.2.2 High- $z$

In Fig. 1.14 we show how the ratio of NIR to UV luminosity depends on the blueshift and rest-frame equivalent width of the C iv line. C iv blueshifts are calculated as in Section XX. We see that the NIR to UV luminosity ratio is strongly correlated with the blue-shift of the C iv emission line. A similar trend was noted by Wang et al., (2013). Interestingly, we note strong similarities to the object subsets selected according to their C iv-emission properties in Richards et al., (2011) (see Figures 11 & 12). We note that the correlation between the hot dust and the C iv emission properties will lead to apparent correlations between the host dust and the BH mass.

*Need to re-do this and understand why beta-related trend is apparently stronger than with the blackbody parameters.*

#### 1.11 DISCUSSION

Roseboom et al., (2013) studied a similar sample of luminous type 1 quasars. They, like us, modelled the NIR emission using a black-body and modelled the emission at longer wavelengths using a clumpy

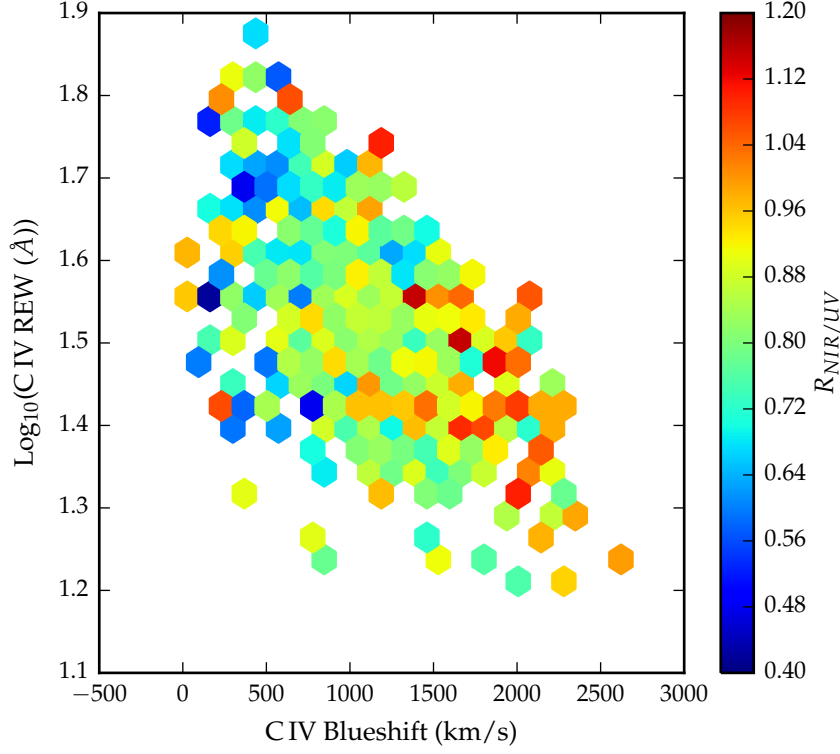


Figure 1.14: Rest-frame equivalent width and blueshift of the C IV line for 7,115 SDSS DR7 quasars. The colours of the hexagons denote the median hot dust ( $T \simeq 1200$  K) abundance for all quasars at a given equivalent width and blueshift. Quasars with the most extreme outflow signatures are predominantly hot-dust rich. Only bins containing a minimum of two objects are plotted.

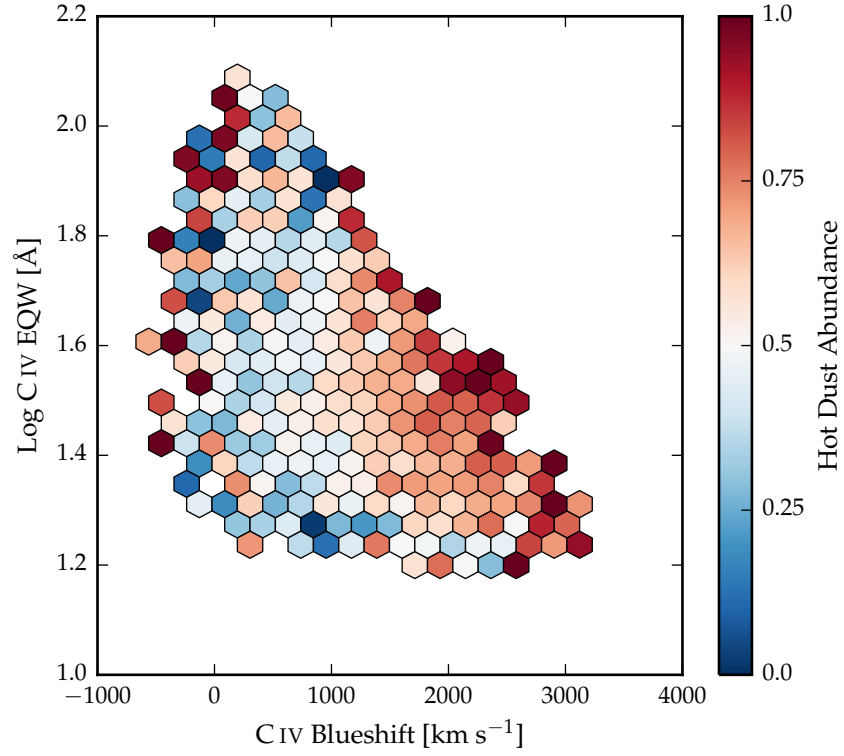


Figure 1.15: Rest-frame equivalent width and blueshift of the C IV line for 7,115 SDSS DR7 quasars. The colours of the hexagons denote the median hot dust ( $T \simeq 1200$  K) abundance for all quasars at a given equivalent width and blueshift. Quasars with the most extreme outflow signatures are predominantly hot-dust rich. Only bins containing a minimum of two objects are plotted. **Change hot dust abundance.**

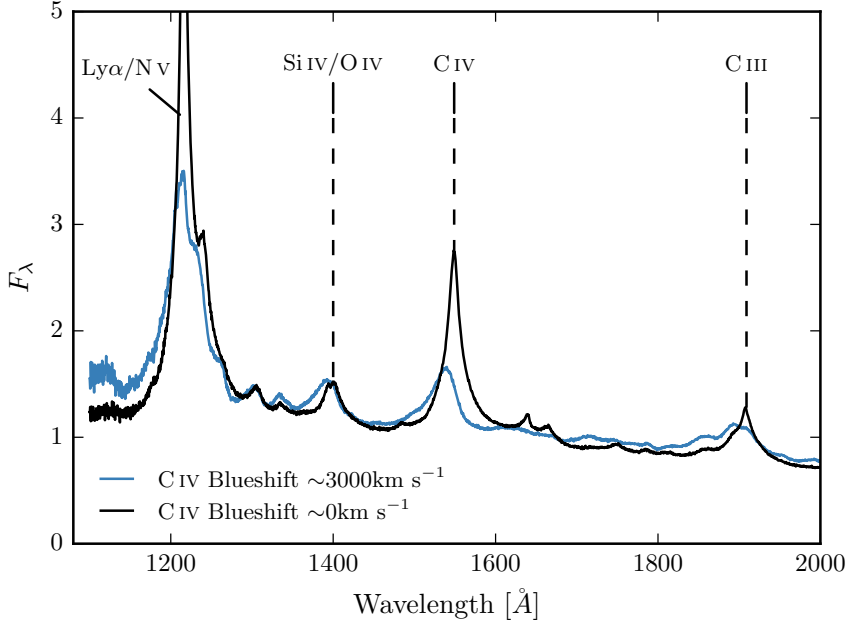


Figure 1.16

torus model. They find that while  $L_{1-5\mu\text{m}}/L_{\text{IR}}$  appears relatively insensitive to  $L_{\text{bol}}$  and  $L_{\text{IR}}$ , a strong correlation appears between  $L_{1-5\mu\text{m}}/L_{\text{IR}}$  and  $L_{\text{IR}}/L_{\text{bol}}$  (i.e. the dust covering factor). They explain this correlation by postulating that as the covering factor of the torus decreases, the maximum inclination at which a type 1 quasar would be seen increases. An increase in the inclination will mean direct sight lines to more of the inner wall of obscuring material closest to the accretion disc.

Mor and Trakhtenbrot, (2011) also looked at the hot dust properties of a sample of  $0.75 < z < 2$  quasars, with photometry from SDSS and WISE. They modelled the NIR emission with hot clouds of pure graphite dust. They reported an anti-correlation between the covering factor of hot dust clouds and the quasar bolometric luminosity. Like us, they neglect cooler dust components which will dominate the SED at longer wavelengths. As we have discovered (see Figure residual plot), the missing flux decreases with redshift because we observe shorter rest-frame wavelengths when the observed spectrum is redshifted to a greater degree. This will induce an anti-correlation between the luminosity of the hot dust component and the luminosity of the quasar (which is correlated with redshift). At  $z=0.75$ , the  $W_3$  band-pass (the longest in their fits) is sensitive to flux from  $6.9\mu\text{m}$ ; at this wavelength we expect the contribution from cooler dust to dominate over the hot dust. It is possible that this effect could explain the

tension with our own result that  $R_{\text{NIR/UV}}$  does not depend on the quasar luminosity in our low- $z$  sample.

Shen and Ho, (2014) quantify the relative torus emission using the  $r - W1$  colour for a sample of  $0.4 < z < 0.8$  SDSS quasars. At these redshifts  $W1$  is observing between 1.9 and 2.4 microns in the rest-frame of the quasar, which suggests that they are sensitive to the same component of hot dust which we are investigating. They observe a mild trend of decreasing relative torus emission as the quasar luminosity increases. We note that their use of the  $r - W1$  at much higher redshifts may be problematic, as the  $W1$  flux will be increasingly dominated by direct emission from the accretion disc.

Gallagher et al., (2007) undertook a similar investigation for a much smaller sample of 234 radio-quiet quasars.

Reverberation measurements of nearby AGNs suggest the near-infrared emission is dominated by hot dust very close to the central source (few tens of light days; e.g. Minezaki et al., 2004; Suganuma et al., 2006). The hot dust signature could contain information about inner face of an obscuring torus structure and/or constrain the dust content of an accretion disc wind. Several studies have shown that the luminosity of the NIR excess emission correlates with that of the central engine with a slope close to unity e.g. Gallagher et al., 2007, suggesting that the dust is reprocessing radiation from the accretion disc.

Outflows may emerge from the outer region of the accretion disc or even the innermost region of the torus, in which the gas clouds are dusty and relatively cold. Indeed, there is observational evidence for dusty outflows close to the central engine (e.g. Bowler et al., 2014). The dust is heated by the central engine, and radiates in the near-infrared band. Wang et al., (2013), fitting the NIR emission with a single power-law, found that objects with strong outflow signatures (blue-shifted C IV) have more hot dust emission relative to the accretion disc emission in a large sample of  $z \sim 2$  non-BAL quasars. It could be that this correlation is induced by a third factor that simultaneously affects outflows and dust emission, for instance the inclination angle or metallicity. Alternatively the dust could be intrinsic to outflows and may have a non-trivial contribution to the outflow acceleration. Also found by Shen and Ho, (2014).

Several other investigations have drawn attention to the rest-frame near-infrared SEDs, with populations of ‘dust free’ objects postulated (Hao et al., 2010; Hao et al., 2011; Jiang et al., 2010; Mor and Trakhtenbrot, 2011)

#### 1.11.1 Eddington ratio

Wang et al., Zhang et al., and Mor & Trakhtenbrot find no significant dependence of the amount of hot dust on the Eddington ratio.

Is this because the Eddington ratio is wrong or because it's more complicated? (can high accretion objects with no evidence for strong outflows.)

#### 1.12 FURTHER WORK

What more is needed to test model(s)?

